APERTURE AND BEAM-TUBE MODELS FOR ACCELERATOR MAGNETS*

H. De Gersem†, Katholieke Universiteit Leuven, Belgium
S. Koch, T. Weiland, Technische Universität Darmstadt, Germany

Abstract

Standard 2D magnetodynamic finite-element models for accelerator magnets are accomplished by dedicated models for the aperture and for the beam-tube end parts. The resulting hybrid and coupled models necessitate the application of specialized algebraic solution techniques in order to preserve the computational efficiency, i.e., matrix-free iterative solvers combined with fast Fourier transforms and Schwarz-type preconditioners.

INTRODUCTION

3D finite-element (FE) models of accelerator magnets may become prohibitive when transient phenomena at small temporal and spatial scale should be resolved, i.e., eddy current effects in windings, beam tube and yoke or filamentary and coupling effects in superconductive cables. Simulation times of several hours have been reported. As a consequence, such calculations are only feasible at later stages of the design process, when geometry, materials and operating conditions are more or less fixed. At an earlier design stage, parameter variations and optimization steps are carried out, almost exclusively on the basis of semi-analytical formulae. It makes sense to support this design phase by FE models that succeed in attaining lower but acceptable accuracies within substantially smaller simulation times, compared to transient 3D simulation [3]. Efforts in the direction of this goal consider 2D FE models where extensions are implemented that deal with typical 3D effects and model some small-scale effects in a problem specific way. In this paper, two extensions for 2D and 3D FE models are proposed. The high-resolution aperture model and the beam-tube end model developed here, both significantly increase the modeling power for superconductive magnets and succeed in keeping the computation time for transient 2D FE simulation as low as a few minutes.

APERTURE MODEL

Domain Decomposition and Mixed Formulation

The magnet geometry is divided in two parts: an outer domain Ω_1 including the windings and yoke and a cylindrical inner domain Ω_2 in the magnet aperture (Fig. 1). The interface is denoted by $\Gamma_{12} = \Omega_1 \cap \Omega_2$. A mixed magneto-quasistatic (MQS) formulation is applied:

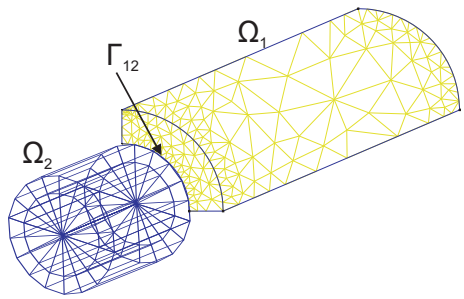

Figure 1: Magnet model: FE mesh for the outer part and tensor-product grid for the aperture.

$$\nabla \times \left(\nu \nabla \times \vec{A}\right) + \sigma \frac{\partial \vec{A}}{\partial t} = \vec{J}_{\mathrm{s}} \quad \text{in } \Omega_1 \; ; \qquad (1)$$

$$-\nabla \cdot (\mu \nabla \psi) = 0 \quad \text{in } \Omega_2 \; , \qquad (2)$$

where $\vec{A}$ is the magnetic vector potential, ψ the magnetic scalar potential, $\vec{J}_{\mathrm{s}}$ the applied current density, μ the permeability, $\nu = 1/\mu$ the reluctivity and σ the conductivity. The normal continuity of the magnetic flux density $\vec{B} = \nabla \times \vec{A} = -\mu \nabla \psi$ and the tangential continuity of the magnetic field strength $\vec{H} = \nu \nabla \times \vec{A} = -\nabla \psi$ are enforced at the interface Γ_{12}. The domains are equipped with different formulations that are dual with respect to each other. The MQS formulation in terms of $\vec{A}$ is capable of considering the eddy current phenomena in the yoke, beam tube and windings, at the expense of being a vectorial partial differential equation (PDE). On the contrary, the MQS formulation in terms of ψ is static but is a scalar formulation. Such so-called *mixed* formulations have been frequently used for MQS simulation in the eighties, especially because of the relatively small number of degrees of freedom which was beneficial for the direct and Krylov-type solvers used at that time [11]. A drawback of a mixed formulation is the fact that the computed magnetic energy and power loss do not converge monotonically with respect to the mesh size as is the case for the non-mixed formulations. The motivation for choosing a mixed formulation will become clear below.

Discretization and System Properties

$\vec{A}$ is discretized in Ω_1 by the standard lowest-order edge elements $\vec{w}_j$, whereas ψ is discretized in Ω_2 by standard

* This work was supported by the Helmholtzzentrum für Schwerionenforschung GmbH (GSI), Darmstadt and by the Katholieke Universiteit Leuven under grant STRT1/09/041.

† herbert.degersem@kuleuven-kortrijk.be

lowest-order nodal elements N_q:

$$\vec{A} = \sum_j u_j \vec{w}_j \quad \text{in } \Omega_1 \; ; \quad \psi = \sum_q v_q N_q \quad \text{in } \Omega_2 \; . \quad (3)$$

where the degrees of freedom (DoFs) for $\vec{A}$ and ψ are stored in the vectors $\mathbf{u}$ and $\mathbf{v}$, respectively. The application of the Ritz-Galerkin approach results in the coupled system of equations

$$\begin{bmatrix} \mathbf{K} + \mathbf{M}\frac{\mathrm{d}}{\mathrm{d}t} & \mathbf{B} \\ \mathbf{B}^T & -\mathbf{G} \end{bmatrix} \begin{bmatrix} \mathbf{u} \\ \mathbf{v} \end{bmatrix} = \begin{bmatrix} \mathbf{f} \\ 0 \end{bmatrix} , \quad (4)$$

further also denoted by $\mathbf{A}\mathbf{x} = \mathbf{b}$ [1]. Eq. (4) is transferred in frequency domain or discretized in time by any implicit time-integration technique. For conciseness, this is not explicitly carried out in the formulae. The matrix entries are

$$\mathbf{K}_{ij} = \int_{\Omega_1} \nu \nabla \times \vec{w}_j \cdot \nabla \times \vec{w}_i \, \mathrm{d}\Omega \; ; \quad (5)$$

$$\mathbf{M}_{ij} = \int_{\Omega_1} \sigma \vec{w}_j \cdot \vec{w}_i \, \mathrm{d}\Omega \; ; \quad (6)$$

$$\mathbf{B}_{iq} = -\int_{\Gamma_{12}} (\nabla N_q \times \vec{w}_i) \cdot \mathrm{d}\vec{\Gamma} \; ; \quad (7)$$

$$\mathbf{G}_{pq} = \int_{\Omega_2} \mu \nabla N_q \cdot \nabla N_p \, \mathrm{d}\Omega \; ; \quad (8)$$

$$\mathbf{f}_i = \int_{\Omega_1} \vec{J}_\mathrm{s} \cdot \vec{w}_i \, \mathrm{d}\Omega \; . \quad (9)$$

The matrices $\mathbf{K}$ and $\mathbf{M}$ are both sparse, symmetric and positive semi-definite. The zero eigenvalues of $\mathbf{K}$ are related to the undetermined gradient fields, whereas the zero eigenvalues of $\mathbf{M}$ are related to the non-conductive model parts. The MQS formulation in terms of the magnetic scalar potential leads to a sparse, symmetric, positive definite system matrix $\mathbf{G}$. The mixed system (4) is sparse, symmetric and indefinite. The indefiniteness is related to the mixed character of the formulation. If the inverse of $\mathbf{G}$ can be obtained or applied in a cheap way, the possibility exists to turn over to the Schur complement system

$$\left(\underbrace{\mathbf{K} + \mathbf{M}\frac{\mathrm{d}}{\mathrm{d}t} + \mathbf{B}\mathbf{G}^{-1}\mathbf{B}^T}_{\mathbf{S}} \right) \mathbf{u} = \mathbf{f} \; . \quad (10)$$

The Schur complement matrix $\mathbf{S}$ is symmetric and positive semi-definite. $\mathbf{S}$ contains large dense blocks due to $\mathbf{G}^{-1}$. Its application in the form of (10) is therefore substantially more expensive than the application of $\mathbf{K} + \mathbf{M}\frac{\mathrm{d}}{\mathrm{d}t}$. The sparsity structure of the Schur complement system is the same as for a FE, boundary-element (BE) coupled formulation where the normal derivatives are eliminated [8].

The mixed system can be solved by the Minimal Residual (MINRES) method [10]. MINRES requires a positive semi-definite preconditioner. As a first choice,

$$\tilde{\mathbf{A}}_1^{-1} = \begin{bmatrix} \tilde{\mathbf{L}}^{-1} & 0 \\ 0 & \tilde{\mathbf{G}}^{-1} \end{bmatrix} \quad (11)$$

is proposed. Here, $\tilde{\mathbf{L}}^{-1}$ denote any possible positive semi-definite approximation to $(\mathbf{K} + \mathbf{M}\frac{\mathrm{d}}{\mathrm{d}t})^{-1}$ such as, e.g., an Incomplete Cholesky (IC) preconditioner or Algebraic Multigrid (AMG) approach. As a second diagonal block, an operator $\tilde{\mathbf{G}}^{-1}$ is used as an approximation to $\mathbf{G}^{-1}$. It has been shown that the convergence of the MINRES method with this preconditioner is not optimal, even if no approximations are used for the diagonal blocks. Better is

$$\tilde{\mathbf{A}}_2^{-1} = \begin{bmatrix} \tilde{\mathbf{S}}^{-1} & 0 \\ 0 & \tilde{\mathbf{G}}^{-1} \end{bmatrix} \quad (12)$$

where $\tilde{\mathbf{S}}^{-1}$ is an approximation to the inverse of $\mathbf{S}$. If no approximations are introduced, this preconditioner causes the MINRES algorithm to converge in exactly 2 iteration steps. The construction of an approximation to $\mathbf{S}$ is not trivial. The *additive Schwarz*-type preconditioner

$$\tilde{\mathbf{S}}_2^{-1} = \left(\mathbf{K} + \mathbf{M}\frac{\mathrm{d}}{\mathrm{d}t} \right)^{-1} + \mathbf{B}\mathbf{G}\mathbf{B}^{-1} \quad (13)$$

is known to be a simple and effective possibility [12]. Alternatively, it is possible to solve (10) by the Conjugate Gradient (CG) method. As preconditioners, either the approximation $\tilde{\mathbf{S}}_1^{-1} = \tilde{\mathbf{L}}^{-1}$ or the approximate inverse $\tilde{\mathbf{S}}_2^{-1}$ to the Schur complement system can be used.

Spectral Resolution and System Representation

The spatial resolution in the aperture can be improved considerably by choosing an orthogonal set of basis functions instead of the set of standard lowest order nodal shape functions $\{N_q\}$. The cylindrical aperture domain $\Omega_2 = [-R, R] \times [0, \pi[\times [-Z, Z]$ has a radius R and a length $2Z$ centered with respect to the $z = 0$ plane. In the spectral-element (SE) approach, basis functions of the form

$$M_q(r, \theta, z) = T_{q_1}\left(\frac{r}{R}\right) \, e^{-\jmath\lambda\theta} \, T_{q_2}\left(\frac{z}{Z}\right) \quad (14)$$

are considered at a cylindrical tensor-product grid (Fig. 1). In the r- and the z-direction, the shape functions vary as Chebyshev functions, whereas in the θ-direction harmonic functions are used. To avoid a clustering of collocation points at the $r = 0$ axis, the r-coordinate is taken from $-R$ to R, the θ-coordinate is restricted to $[0, \pi[$ and an even number of collocation points is used in the r-direction. The matrices $\mathbf{B} = \mathbf{Z}^T\mathbf{Q}^T\hat{\mathbf{D}}$ and $\mathbf{G} = \mathbf{D}^H\mu\mathbf{D}$ are available in factorized form. Here, $\mathbf{Z}$ interpolates the fictitious interface currents between the spectral collocation points of the tensor-product grid and the edges of the FE mesh, $\mathbf{Q}$ selects the spectral DoFs at the collocation points at the interface, $\mathbf{D} = [\; \mathbf{D}_r \quad \mathbf{D}_\theta \quad \mathbf{D}_z \;]^H$ and $\mathbf{D}_r$, $\mathbf{D}_\theta$ and $\mathbf{D}_z$ are the spectral differentiation matrices along r, θ and z. The particular choice of the collocation points allow to invoke each of these differentiation matrices by means of the Fast Fourier Transform (FFT):

$$\mathbf{D}_r = \mathbf{D}_\theta = \mathbf{D}_z = \mathbf{F}^{-1}\mathbf{U}\mathbf{F} \; , \quad (15)$$

where $\mathbf{U}$ is a diagonal matrix [13]. The spectral differentiation matrices are fully populated. The operator $\mathbf{Q}$ can be represented by an index set. The interpolation operator $\mathbf{Z}$ is stored in a sparse matrix format. The coupling matrix $\mathbf{B}$ has a sparse row structure related to the FE DoFs and a dense column structure related to the SE DoFs. The Schur-complemented FE-SE system is comparable to a FE-BE coupled system [8] and equivalent to the FE system in which the SE domains are considered as specialized Robin-type boundary conditions applied at Γ_{12} [2].

A SE discretization is known to attain an exponential convergence of the discretization error with respect to the number of DoFs. Because a part of the model remains discretized by FEs, the convergence of the overall model is limited to the convergence of the FE part. Nevertheless, the SE discretization of the aperture allows to considerably reduce the number of DoFs required to sufficiently resolve the aperture field.

During the system-solving phase, most of the computation time is spent to the multiplication by the system matrix and the application of the preconditioner. Commonly, the matrices $\mathbf{A}$ and $\mathbf{S}$ are stored in a compressed way. The preconditioner steps are available by operations on the fly making use of the stored system matrices. This may become inefficient for the coupled FE-SE matrices which are substantially more dense than their pure FE counterparts. The use of properly located collocation points allows for the use of FFTs. Then, only the operations $\mathbf{K} + \mathbf{M}\frac{\mathrm{d}}{\mathrm{d}t}$, $\tilde{\mathbf{L}}^{-1}$ and $\mathbf{Z}$ are carried out using a sparse storage system. $\mathbf{Q}$ corresponds to selecting a subset of the DoFs of $\mathbf{v}$ using an index set. Now, the matrices $\mathbf{A}$ and $\mathbf{S}$ are no longer given explicitly and pure algebraic preconditioning techniques such as e.g. IC, are no longer available. The preconditioners $\tilde{\mathbf{A}}_1^{-1}$, $\tilde{\mathbf{A}}_2^{-1}$, $\tilde{\mathbf{L}}^{-1}$ and $\tilde{\mathbf{S}}_2^{-1}$, however, remain available.

The expected computational effort of a pure FE model is of order $\mathcal{O}(n^3)$, where n is a measure for the number of DoFs counted along one spatial direction. This complexity is related to the application of $\mathbf{K}$, $\mathbf{M}$ and $\tilde{\mathbf{L}}^{-1}$. The application of 2D FFTs scales like $\mathcal{O}(n^2 \ln n)$ which is asymptotically below $\mathcal{O}(n^3)$. Hence, the complexity of the coupled FE-SE model is expected to be comparable to the complexity of a pure FE model. This is no longer true when the coupling matrices $\mathbf{B}$ and spectral system matrix $\mathbf{G}$ are represented by algebraic matrices. The full population of $\mathbf{B}$ and $\mathbf{G}$ causes their application to scale by $\mathcal{O}(n^4)$, which would dominate the overall calculation.

Numerical Experiments

The different iterative solution techniques are compared for a 2D quarter model of a superconductive dipole magnet. The iron yoke is substantially saturated. The yoke and the windings are discretized by FEs where the aperture is discretized by the spectral basis functions $M_q(r,\theta) = T_{q_1}\left(\frac{r}{R}\right) e^{-\jmath\lambda\theta}$. The SE technique supports an easy calculation of the harmonic field coefficients that determine the quality of the accelerator magnet.

Table 1: Computation times (in seconds) for the proposed iterative solution methods for the mixed FE-SE system and the Schur complement system using the compressed row storage (CRS) form or the matrix-free solution techniques techniques; comparison with respect to a homogeneous FE model used as a reference (indicated by the subscript "ref"); approximation to FE system matrices are created using the IC technique without fill-in.

model	system	solver	precond.	CRS	matrix-free
FE	$\mathbf{L}_{\mathrm{ref}}$	CG	$\tilde{\mathbf{L}}_{\mathrm{ref}}^{-1}$	27.23	-
FE-SE	$\mathbf{A}$	MINRES	$\tilde{\mathbf{A}}_1^{-1}$	9.06	11.02
FE-SE	$\mathbf{A}$	MINRES	$\tilde{\mathbf{A}}_2^{-1}$	8.55	7.56
FE-SE	$\mathbf{S}$	CG	$\tilde{\mathbf{S}}_1^{-1}$	78.34	5.58
FE-SE	$\mathbf{S}$	CG	$\tilde{\mathbf{S}}_2^{-1}$	55.34	3.25

As an approximation to the FE system part, an IC factorization without fill-in is used. The performance of the proposed solution techniques is compared in Table 1, both in the case where the system is assembled into a compressed row storage (CRS) format and used in matrix form as in the case where matrix-free techniques and FFTs are applied. The experiments clearly illustrate the computational efficiency of the matrix-free techniques. The FFTs solving the SE subproblem are responsible for less than 10% of the overall computation time. The experiments show that solving the positive semi-definite Schur complement system is more efficient than solving the mixed system, as long as matrix-free techniques are used. The numerical tests indicate the advantage of a additive-Schwarz-type preconditioner over a preconditioner only accounting for the FE part. When carried out using matrix-free techniques, all hybrid FE-SE discretizations outperform the model with a pure FE discretization attaining a comparable spatial resolution.

BEAM-TUBE MODEL

Beam-Tube Modeling

The beam tube in an accelerator magnet consists of a thin pipe with a circular or elliptical cross-section. The beam tube should support the inner vacuum and is commonly made of conductive material in order to carry a blind current. During the ramping of the magnet, eddy currents are generated in the beam tube. These currents cause additional losses and may deteriorate the quality of the aperture field. The calculation of these eddy currents necessitates transient simulation, which is time consuming, particularly in combination with 3D FE models [5]. Explicitly resolving the beam-tube thickness is commonly avoided in order to restrict the model size. Moreover, as accelerator magnets exhibit a translational symmetry, relevant simulation results can already be generated on the basis of 2D FE models. A 2D model is not capable of modeling the closing paths of the beam-tube eddy currents at the front and back

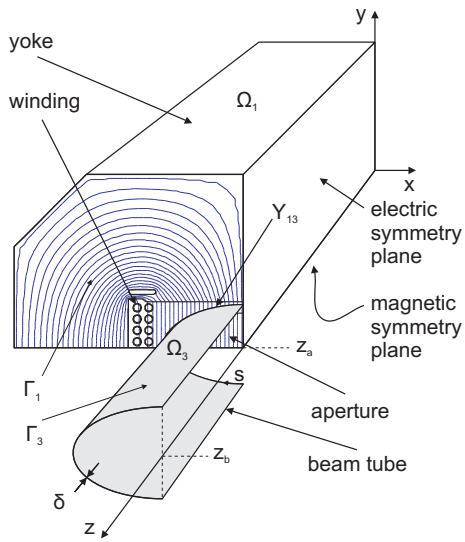

Figure 2: Accelerator magnet with beam tube: computational domain and magnetic flux lines.

side of the accelerator magnet. These closing paths are expected to have a significant influence on the distribution of eddy currents along the circumference of the beam-tube cross-section. This section is dedicated to the addition of a model part accounting for these closing paths.

2D FE Model and Thin-Sheet Approximation

The central part Ω_1 of the accelerator magnet is translationally symmetric along the z-direction: $\Omega_1 = \Gamma_1 \times \ell_z$ where Γ_1 is the cross-section and ℓ_z is the length along the z-direction (Fig. 2). The translational symmetry of Ω_1 is reflected in the choice of the edge shape functions $\vec{w}_j$ for discretizing the magnetic vector potential $\vec{A}$:

$$\vec{w}_j = \frac{N_j(x,y)}{\ell_z}\vec{e}_z \tag{16}$$

where $N_j(x,y)$ are lowest-order nodal shape functions defined at a triangularization of Γ_1 and $\vec{e}_z$ is a unit vector in the z-direction.

The thickness δ of the beam tube is much smaller than the skin depth

$$\delta_{\text{skin}} = \sqrt{\frac{2}{\omega\sigma_{\text{tube}}\mu_{\text{tube}}}}\,. \tag{17}$$

related to the beam-tube conductivity σ_{tube} and permeability μ_{tube} and expected for the relevant angular frequencies ω. This allows to assume a current density which is homogeneously distributed along the beam-tube thickness. The cross-section of the beam tube with Γ_1 can be represented by $\Upsilon_{\text{tube}} \times [-\frac{\delta}{2}, \frac{\delta}{2}]$ where Υ_{tube} is a contour in Γ_1 (Fig. 2). The beam-tube cross-section is not explicitly resolved by the mesh. The eddy currents in the beam tube are included by augmenting the conductance matrix $\mathbf{M}_\sigma$ with the line integrals

$$\mathbf{M}^{\text{thin}}_{\sigma,ij} = \int_{\Upsilon_{\text{tube}}} \sigma_{\text{tube}}\vec{w}_j \cdot \vec{w}_i \delta\ell_z \; \mathrm{d}s \tag{18}$$

where σ_{tube} is the conductivity of the beam-tube material. This approach corresponds to the most simple form of a thin-sheet model [9, 7]. In this paper, this 2D thin-sheet model is accomplished by an additional treatment for modeling the closing paths of the beam-tube current.

End Effects

End effects are the effects due to the broken translational symmetry at the front and rear sides of the model. In the center of the magnet, the beam-tube eddy currents are perpendicular to the magnet cross-section. At the end parts, some of the current lines may proceed to the next magnet and other current lines may close in a more or less circular path on the surface of the beam tube. The fact that the different closing paths feature a different impedance, disturbs the translational symmetry of the model. The constructed 2D FE model considers a perfectly conductive connection at the front and rear end. Several approaches exist to account for the additional impedances of the closing paths, while sticking to a 2D model. A common approximation is to consider the beam-tube parts exceeding the magnetically active part by decreasing the conductivity of the beam-tube material, i.e.,

$$\sigma_{\text{tube}} \rightarrow \sigma_{\text{tube}}\frac{\ell_z + \ell_{\text{end}}}{\ell_z} \tag{19}$$

where ℓ_{end} denotes the length of the outside beam-tube parts. This approach does not account for the considerably longer closing paths of the beam-tube currents at the magnetic symmetry plane compared to those at the electric symmetry plane (Fig. 2).

Beam-Tube End Model

Besides the magnetically active model part $\Omega_1 = \Gamma_1 \otimes [0, z_a]$, an additional domain $\Omega_3 = \Gamma_3 \otimes [-\frac{\delta}{2}, +\frac{\delta}{2}]$ is considered (Fig. 2). Here, $\Gamma_3 = \Upsilon_{\text{tube}} \otimes [z_a, z_b]$ is the beam-tube surface outside the active magnet part. By construction, the intersection of both domain parts is $\Omega_1 \cap \Omega_3 = \Upsilon_{\text{tube}} \otimes [-\frac{\delta}{2}, +\frac{\delta}{2}]$. The coupled formulation reads

$$\nabla \times \left(\nu\nabla \times \vec{A}\right) + \sigma\frac{\partial \vec{A}}{\partial t} + \sigma\nabla\varphi = \vec{J}_{\text{s}} \quad \text{in } \Omega_1 \tag{20}$$

$$-\nabla \cdot \left(\sigma\frac{\partial \vec{A}}{\partial t}\right) - \nabla \cdot (\sigma\nabla\varphi) = 0 \quad \text{in } \Omega_3 \tag{21}$$

where φ is the electric scalar potential. In Ω_1, the electromagnetic field is computed by (20), incorporating both inductive and resistive field effects. In Ω_3, the inductive effects are neglected with respect to the resistive effects. This allows to use the stationary-current formulation.

Discretization

The applied FE shape functions are

$$\begin{array}{rcll} \vec{w}_j(x,y,z) & = & \frac{N_j(x,y)}{z_a}\vec{e}_z & \text{in } \Omega_1 \ ; \\ P_{\tilde{q}}(s,z) & = & M_{\tilde{q}}(s,z_a)\frac{z}{z_1} & \text{in } \Omega_1 \ ; \\ P_q(s,z) & = & M_q(s,z) & \text{in } \Omega_2 \end{array} \tag{22}$$

where $N_j(x,y)$ and $M_q(s,z)$ are nodal shape functions defined on triangulations of Γ_1 and Γ_3, respectively (Fig. 2). The indices $i,j \in \mathcal{I}_1$, $p,q \in \mathcal{I}_3$ and $\tilde{p},\tilde{q} \in \mathcal{I}_1 \cap \mathcal{I}_3$ and the index sets $\mathcal{I}_1$, $\mathcal{I}_3$ and $\mathcal{I}_1 \cap \mathcal{I}_3$ refer to the nodes of Γ_1, Γ_3 and $\Upsilon_{\text{tube}} = \Gamma_1 \cap \Gamma_3$, respectively. The potentials are

$$\left\{ \begin{array}{rcl} \vec{A} & = & \sum_j u_j \vec{w}_j \\ \varphi & = & \sum_{\tilde{q}} v_{\tilde{q}} P_{\tilde{q}} \end{array} \right. \quad \text{in} \quad \Omega_1 \ ; \tag{23}$$

$$\left\{ \begin{array}{rcl} \vec{A} & = & 0 \\ \varphi & = & \sum_q v_q P_q \end{array} \right. \quad \text{in} \quad \Omega_3 \ , \tag{24}$$

where the DoFs are gathered in the algebraic vectors $\mathbf{u}$ and $\mathbf{v}$. The DoFs $v_{\tilde{q}}$ are a subset of all DoFs v_q. They share the shape functions $P_{\tilde{q}}$ defined in Ω_1 and P_q defined in Ω_3 and therefore enforce the continuity of φ at Υ_{tube}.

The FE shape functions serve for discretizing (20) and (21) at Ω_1 and Ω_3, respectively. Eq. (20) is weighted by $\vec{w}_i$ whereas (21) is weighted by the functions P_q. The resulting coupled system of equations reads

$$\left[\begin{array}{cc} \mathbf{K} + \mathbf{M}\frac{\mathrm{d}}{\mathrm{d}t} & \mathbf{B}^T \\ \mathbf{B}\frac{\mathrm{d}}{\mathrm{d}t} & \mathbf{G} \end{array} \right] \left[\begin{array}{c} \mathbf{u} \\ \mathbf{v} \end{array} \right] = \left[\begin{array}{c} \mathbf{f} \\ \mathbf{0} \end{array} \right] \tag{25}$$

where

$$\mathbf{K}_{i,j} = \int_{\Gamma_1} \left(\frac{\nu_y}{z_a}\frac{\partial N_i}{\partial x}\frac{\partial N_j}{\partial x} + \frac{\nu_x}{z_a}\frac{\partial N_i}{\partial y}\frac{\partial N_j}{\partial y} \right) \mathrm{d}A \ ;$$

$$\mathbf{M}_{i,j} = \int_{\Gamma_1} \frac{\sigma}{z_a} N_i N_j \, \mathrm{d}A \ ; \tag{26}$$

$$\mathbf{f}_i = \int_{\Gamma_1} J_{\mathrm{s},z} N_i \, \mathrm{d}A \ ; \tag{27}$$

$$\mathbf{B}_{\tilde{p},j} = \int_{\Upsilon_{\text{tube}}} \frac{\sigma}{z_a} M_{\tilde{p}} N_j \delta \, \mathrm{d}s \ ; \tag{28}$$

$$\mathbf{G} = \int_{\Gamma_3} \sigma \nabla_{\Gamma_3} M_p \cdot \nabla_{\Gamma_3} M_q \delta \, \mathrm{d}A \ . \tag{29}$$

Here, ∇_{Γ_3} denotes a gradient operator accounting for the curvature of Γ_3. This system is symmetric and positive definite and can be solved by a preconditioned CG method.

Also here, it is possible to eliminate the additional degrees of freedom $\mathbf{v}$ related to φ from the system. The resulting Schur complement system reads

$$\mathbf{K}\mathbf{u} + \left(\mathbf{M} - \mathbf{B}^T\mathbf{G}^{-1}\mathbf{B}\right)\frac{\mathrm{d}\mathbf{u}}{\mathrm{d}t} = \mathbf{f} \ . \tag{30}$$

The matrix $\mathbf{M}_{\text{schur}} = \mathbf{M} - \mathbf{B}^T\mathbf{G}^{-1}\mathbf{B}$ can be interpreted as a modified FE conductance matrix accounting for the closing paths outside of the 2D cross-sectional model. It is easily shown that $\mathbf{M}_{\text{schur}}$ is symmetric and positive semi-definite, similar to $\mathbf{M}$. Solving (30) can be done by a preconditioned CG method, but may be computationally expensive because of the dense blocks $\mathbf{B}^T\mathbf{G}^{-1}\mathbf{B}$.

SIMULATION RESULTS

The additional aperture and beam-tube end model parts are applied in combination with a transient simulation of the SIS-100 superconductive magnet which is part of the Facility for Antiproton and Ion Research (FAIR) project of the Helmholtzzentrum für Schwerionenforschung (GSI) in Darmstadt, Germany [6]. The eddy-current losses in the yoke have already been reported in e.g. [4]. 3D simulations for the beam-tube losses have been studied in [5]. This paper is concerned with 2D simulations providing a comparable accuracy at a significant lower computational costs.

The elliptical cross-section of the beam-tube domain is parametrized by (ξ,η,z), i.e., $(x,y,z) = (\rho\cosh\xi\cos\eta, \rho\sinh\xi\sin\eta, z)$. The corresponding Laplace-Beltrami operator is

$$\nabla^2_{\Omega_3} = \frac{1}{\rho^2\left(\cosh^2\xi - \cos^2\eta\right)}\frac{\partial^2\varphi}{\partial\eta^2} + \frac{\partial^2\varphi}{\partial z^2} \ . \tag{31}$$

The discretization of the model is carried out as described above. The duty cycle of magnet operations is shown in Fig. 3a. During the ramping of the aperture field, eddy currents are induced in the beam tube. The final mesh obtained after a few adaptive mesh refinement steps as well as the magnetic flux lines are shown in Fig. 3d. Fig. 3e and Fig. 3f compare the equipotential lines for the electric scalar potential φ and the arrows for the electric field strength for the connected and unconnected cases, respectively. The figures correspond to the coordinate system (ξ,z) and show a flat projection of the beam-tube surface seen from above. The top side of the figure corresponds to the interface Υ_{tube} between both model parts. The left and right sides fall together with the magnetic symmetry plane. The vertical center line falls together with the electric symmetry plane. The bottom side of the figure corresponds to the connection of the beam tube to the next-in-line accelerator component. The closing paths of the beam-tube currents outside the magnetically active part depend on the fact whether an electric connection exists to the following component of not (compare Fig. 3e to Fig. 3f). The influence of this connection seems to be negligible. Nevertheless, the difference between the results for the model with perfectly conductive front and rear planes and the results for the model with the additional beam-tube end model, are significant, which indicates the relevance of the beam-tube end model. The double 2D model is substantially more efficient than a full 3D model. Therefore, the computational resources can be spent to achieve a finer resolution in the cross-sectional plane, e.g. to tackle the severe ferromagnetic saturation of the magnet yoke (Fig. 3d). The beam-tube losses for the duty cycle of Fig. 3a are shown in Fig. 3b. The dependence of the losses on time is mostly constant because the aperture field is ramped at a constant rate. Due to the saturation in the middle of the duty cycle, the magnetic flux density does not increase further at linear rate, which explains the slightly smaller beam-tube losses.

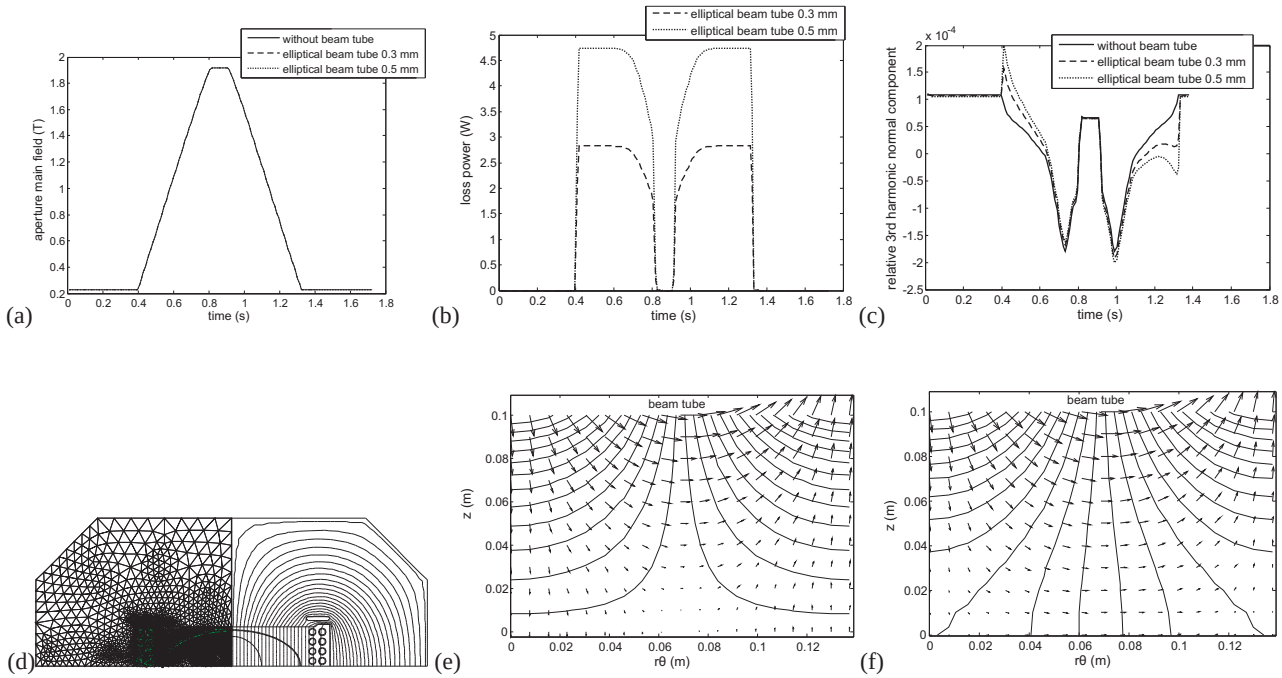

Figure 3: Transient simulation results for the SIS-100 magnet: (a) magnetic flux density in the aperture; (b) power loss; (c) sextupole field component; (d) mesh and magnetic flux lines at maximal aperture field; (e-f) distribution of the current on the beam-tube end surface with (e) and without (f) electric connection to the next magnet.

The beam-tube eddy currents have a disadvantageous effect on the quality of the aperture field as is clear for the sextupole component from Fig. 3c.

CONCLUSION

A cheap transient 2D FE model for accelerator magnets becomes valuable by increasing the resolution of the aperture by a SE discretization and by including end effects in the beam tube by an additional 2D model. The relevance of this technique is given by the fact that the overall transient simulation only takes a few minutes of calculation time and, hence, can be inserted in a flexible design process.

REFERENCES

[1] S.C. Brenner and L.R. Scott. *The Mathematical Theory of Finite Element Methods*. Springer Verlag, New York, 1996.

[2] H. De Gersem and K. Hameyer. Harmonic boundary conditions for circular inclusions and their coupling to external circuits. *IEE Proc.-Sci. Meas. Technol.*, 148(6):257–262, November 2001.

[3] T. Hemker, Oskar von Stryk, H. De Gersem, and T. Weiland. Mixed-integer nonlinear design optimization of a superconductive magnet with surrogate functions. *IEEE Trans. Magn.*, 44(6):1110–1113, June 2008.

[4] S. Koch, H. De Gersem, T. Weiland, E. Fischer, and G. Moritz. Transient 3D finite element simulations of the SIS100 magnet considering anisotropic, nonlinear material models for the ferromagnetic yoke. *IEEE Trans. Appl. Superconduct.*, 18(2):1601–1604, June 2008.

[5] S. Koch, J. Trommler, H. De Gersem, and T. Weiland. Modeling thin conductive sheets using shell elements in magnetoquasistatic field simulations. *IEEE Trans. Magn.*, 45(3):1292–1295, March 2009.

[6] A.D. Kovalenko, A. Kalimov, H.G. Khodzhibagiyan, G. Moritz, and C. Mühle. Optimization of a superferric nuclotron type dipole for the GSI fast pulsed synchrotron. *IEEE Trans. Appl. Superconduct.*, 12(1):161–165, 2002.

[7] L. Krähenbühl and D. Muller. Thin layers in electrical engineering. example of shell models in analyzing eddy-currents by boundary and finite element methods. *IEEE Trans. Magn.*, 29(5):1450–1455, 1993.

[8] S. Kurz, S. Russenschuck, and N. Siegel. Accurate calculation of fringe fields in the LHC main dipoles. *IEEE Trans. Appl. Superconduct.*, 10(1):85–88, March 2000.

[9] T. Nakata, N. Takahashi, K. Fujiwara, and Y. Shiraki. 3-D magnetic field analysis using special elements. *IEEE Trans. Magn.*, 26(5):2379–2381, September 1990.

[10] C.C. Paige and M.A. Saunders. Solution of sparse indefinite systems of linear equations. *SIAM J. Numer. Anal.*, 12(4):617–629, 1975.

[11] P.P. Silvester and R.L. Ferrari. *Finite Elements for Electrical Engineers*. Cambridge University Press, Cambridge, 2nd edition, 1996.

[12] B.F. Smith, P.E. Bjørstad, and W.D. Gropp. *Domain Decomposition: parallel multilevel methods for elliptic partial differential equations*. Cambridge University Press, Cambridge, 1996.

[13] L.N. Trefethen. *Spectral Methods in Matlab*. SIAM, Philadelphia, 2000.